Counting statistics of chaotic resonances at optical frequencies: Theory and experiments

Domenico Lippolis,[1,*] Li Wang,[2] and Yun-Feng Xiao[2,3,†]
[1]*Institute for Applied Systems Analysis, Jiangsu University, Zhenjiang 212013, China*
[2]*State Key Laboratory for Mesoscopic Physics and School of Physics, Peking University; Collaborative Innovation Center of Quantum Matter, Beijing 100871, China*
[3]*Collaborative Innovation Center of Extreme Optics Taiyuan 030006, Shanxi, China*
(Received 7 December 2016; revised manuscript received 8 April 2017; published 18 July 2017)

A deformed dielectric microcavity is used as an experimental platform for the analysis of the statistics of chaotic resonances, in the perspective of testing fractal Weyl laws at optical frequencies. In order to surmount the difficulties that arise from reading strongly overlapping spectra, we exploit the mixed nature of the phase space at hand, and only count the high-Q whispering-gallery modes (WGMs) directly. That enables us to draw statistical information on the more lossy chaotic resonances, coupled to the high-Q regular modes via dynamical tunneling. Three different models [classical, Random-Matrix-Theory (RMT) based, semiclassical] to interpret the experimental data are discussed. On the basis of least-squares analysis, theoretical estimates of Ehrenfest time, and independent measurements, we find that a semiclassically modified RMT-based expression best describes the experiment in all its realizations, particularly when the resonator is coupled to visible light, while RMT alone still works quite well in the infrared. In this work we reexamine and substantially extend the results of a short paper published earlier [L. Wang *et al.*, Phys. Rev. E **93**, 040201(R) (2016)].

DOI: 10.1103/PhysRevE.96.012217

I. INTRODUCTION

Confinement and manipulation of photons using whispering gallery mode (WGM) microcavities [1–3] have triggered intense research due to their unique features, such as the long photon lifetime and strong field confinement. By breaking the rotational symmetry of the WGM microcavities [4], it was recently found that the deformed microcavities not only gain directionality, highly desirable for microlasers and other photonics applications [5–15], but also serve as dynamical billiards for experimentally testing the systems with a mixed phase space, from which one can study classical and quantum chaos [16,17]. In particular, prominent phenomena were so far demonstrated experimentally in the optical microcavity system, e.g., dynamical tunneling [10,18–20], dynamical localization [21,22], scarring [23–25], turnstile transport [26], and avoided resonance crossings [27].

The study of quasibound states (resonances), of importance to understand the mechanisms of chaotic scattering [28–31], is not so often performed on dielectric microcavities [32]. That is due to both experimental and theoretical challenges. On the experimental side, chaotic resonances are often very lossy, and tend to overlap in the spectrum, making recognition problematic [33]. From a theoretical standpoint, the observations may lend themselves to multiple interpretations [34–36], due to the *partial* openness of the system, which makes the wave-ray correspondence highly nontrivial [37].

In the present work we propose a solution to the above problems, by employing a silica-made microcavity (Fig. 1; also see Ref. [38]), which is approximately two-dimensional, has a deformed circular boundary, and is placed on the top of a silicon-made, fully absorbing pedestal.

The ray dynamics inside the resonator, which can be regarded as a leaky billiard, is mixed: while the chaotic dynamics mostly dwells in the central region, the regular (quasiperiodic) rays closely follow the boundary and thus live in the outer toroid. Although there is no physical boundary dividing these two regions of the cavity, regular and chaotic dynamics are well separated in the phase space (Fig. 2) by a KAM boundary [39], so that no classical trajectory can cross between the two. Quantum mechanically, however, a wave localized on one region of the phase space may tunnel into the other [40], so that, generally, overlapping chaotic resonances are coupled to sharp, nonoverlapping regular (WGM) ones [41], and counting the latter from the transmission spectrum can help us draw information on the statistics of the former. That is the basic strategy we adopt to avoid the problem of reading overlapping spectra.

Moreover, the microresonator used here is fabricated on the top of a silicon pillar of smaller radius, which fully absorbs virtually every ray that travels directly above it. Consequently, the system acquires a full opening, and the present experiments may be used to validate existing predictions for the statistics of chaotic resonances.

With these premises, the experiments performed here are aimed at estimating the number of *chaotic* resonances from the sole observation of *regular* ones, mostly WGMs. A thorough analysis is also presented, where we test three different models against the experimental data: (1) a classical prediction, solely based on ray dynamics, (2) a known expression [42] obtained from the truncation of random matrices, and (3) a semiclassical correction [43] to (2), which depends on the Lyapunov exponent of the chaotic dynamics, and therefore on system-specific properties. Theory, methods, experimental conditions, and statistical analysis are explained in full detail.

The method we introduce is intended to set the stage for more general investigations of chaotic scattering phenomena in open systems, beginning with a test at optical frequencies of the fractal Weyl law for the scaling of the number of resonances

*domenico@ujs.edu.cn
†www.phy.pku.edu.cn/~yfxiao/

 ©2017 American Physical Society

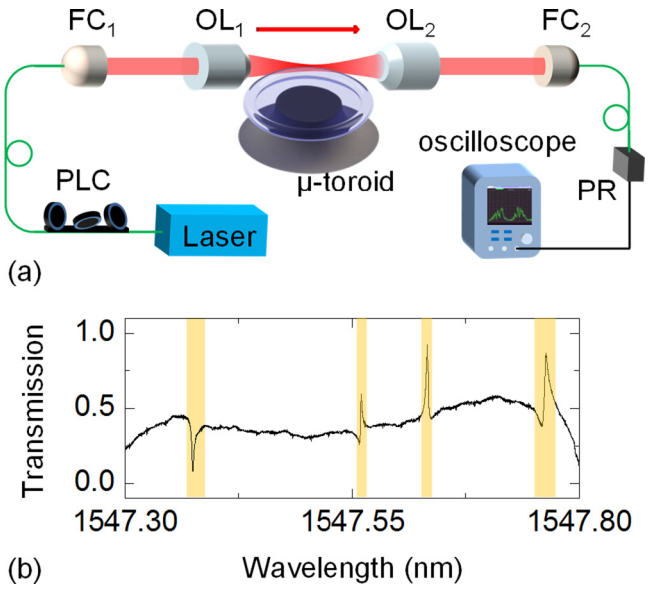

FIG. 1. (a) Schematic representation of the free-space coupled cavity system: the cavity field is excited by visible or infrared laser, while the transmitted signal is detected by an oscilloscope. Key: PLC = polarization controller; FC = fiber coupler; OL = optical lens; PR = photon receiver. (b) A typical transmission spectrum with the high-Q regular modes highlighted.

with the energy [44]. At present, the scaling exponent in this prediction is also believed to depend upon the cutoff chosen for the linewidth [32,45] of the resonances counted, and thus on the range of decay times of the corresponding chaotic states. With that in mind, an important aspect of the present analysis is that to estimate the typical decay time that the experiments are sensitive to. A comparison of the measured maximum escape rates of the chaotic states with the estimated Ehrenfest time of quantum-to-classical correspondence [46] provides useful information in that respect.

The paper is organized as follows. Section II contains the theoretical model, with the equations that couple chaotic to regular modes, obtained with two different but equivalent approaches (Secs. II A and II B, respectively). The key relation between number of chaotic modes and probability of excitation of one regular mode is derived in Sec. II C. The statistics of chaotic modes is treated in Sec. II D with different models, that depend on the time scales involved. In Sec. III A we place an absorber at the center of the cavity to obtain a full opening. Varying the size of the absorber affects the mean dwell time of the chaotic rays from the cavity. A theoretical study of the statistics of resonances and the number of regular modes excited as a function of the radius of the absorber is presented in Sec. III B, while in Sec. III C we numerically investigate the time scale of transient chaos versus escape to the absorber in the ray dynamics. The experimental apparatus is described in Sec. IV, together with the techniques employed to perform measurements of the transmission spectra, and numerical studies of the propagation of both chaotic modes and WGMs inside the cavity. Section V contains the experimental results and their statistical analysis: regular modes are counted in various experimental conditions, and the three different models are validated against the data (Secs. V A and V B).

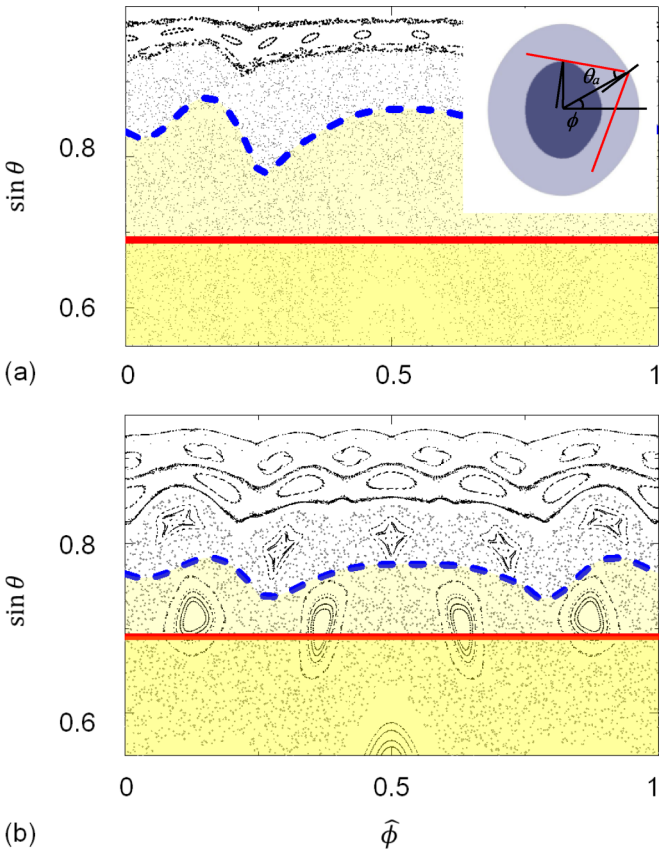

FIG. 2. (a) (inset) Sketch of the deformed microcavity with an inner absorber, characterized by the angle θ_a, and (main) corresponding Poincaré surface of section ($\hat{\phi} \equiv \phi/2\pi$) with deformation factor $\eta = 11.7\%$. The solid red line indicates the angle of total internal reflection, while the dashed curve is given by an absorption angle θ_a such that $r \simeq 0.85$. Different shades of color indicate loss to the absorber (lighter) and by refraction into air (darker). (b) Poincaré section of the microcavity with $\eta = 4.2\%$. The dashed curve is given by an absorption angle θ_a such that $r \simeq 0.77$.

We discuss the proportionality between the probability of excitation of a single regular mode and the number of excited regular modes in Sec. VI. As an independent test of the theory, we also count statistics of the linewidths of the excited regular modes. Conclusions and discussion follow in Sec. VII.

II. THEORETICAL MODEL

Classically, a deformed microcavity allows for both regular and chaotic motion (Fig. 2), which are well separated, so that no trajectory can cross between them. In the quantum picture, however, it is possible for a wave living in one region to leak into the other via dynamical tunneling [40], which introduces a coupling between regular and chaotic resonances.

A. Mode-mode coupling theory

The polarized field [Transverse Electric (TE) or Transverse Magnetic (TM)], excited by the incident beam inside the microcavity, is written as a superposition of one regular (ω)

and several (n) chaotic modes [47]:

$$\psi(x,t) = a_\omega(t)c_\omega(x)e^{ik_\omega z - i\omega t} + \sum_n b_n(t)c_n(x)e^{ik_n z - i\omega_n t}. \quad (1)$$

As said, the regular mode is coupled to the chaotic ones via dynamical tunneling, and therefore, one can write a system of response equations [48] under the slowly varying amplitude assumption [49], and integrate out the spatial part of the modes, to obtain

$$\ddot{b}_n + \omega_n^2 b_n + \gamma_n \dot{b}_n = f_n E_0 - V_n a_\omega, \quad (2a)$$

$$\ddot{a}_\omega + \gamma_\omega \dot{a}_\omega + \omega^2 a_\omega = \sum_n V_n b_n. \quad (2b)$$

Here f_n is the coupling strength of the nth chaotic mode with the laser beam of amplitude E_0 and frequency ω_0. V_n (assumed real) is the coupling strength of the nth chaotic mode with the regular mode, while γ_n and γ_ω are damping rates. Assuming that $\omega_n \approx \omega_0$, one can first set

$$b_n = \mathrm{Re}[b_n e^{-i\omega_0 t}], \quad (3a)$$

$$a_\omega = \mathrm{Re}[a_\omega e^{-i\omega_0 t}] \quad (3b)$$

and then rewrite Eqs. (2) as [38]

$$\dot{b}_n + \gamma_n b_n = f_n E_0 - V_n a_\omega, \quad (4a)$$

$$\dot{a}_\omega + [\gamma_\omega + i(\omega_0 - \omega)]a_\omega = \textstyle\sum_n V_n b_n. \quad (4b)$$

We are interested in the steady-state solution, obtained by setting $\dot{a}_\omega = \dot{b}_n = 0$. The amplitude a_ω of the envelope of the regular mode is found to be [38]

$$a_\omega = \frac{E_0 \sum_n f_n \frac{V_n}{\gamma_n}}{[\gamma_\omega + i(\omega - \omega_0)] + \sum_n \frac{V_n^2}{\gamma_n}}. \quad (5)$$

B. An alternative approach

The same equation may be derived in a different way [50,51]. Consider a Hamiltonian H_0 modeling the closed billiard, whose eigenstates $|a_\omega\rangle$ and $|b_n\rangle$ represent the regular- and chaotic states respectively, uncoupled to one another. The coupling is introduced by the opening, that modifies the Hamiltonian to the non-Hermitian $H = H_0 + V$. Moreover, an incident beam of amplitude E is shone into the cavity. We begin by writing an eigenfunction of H as the superposition

$$|\psi\rangle = a_\omega|a_\omega\rangle + \sum_n b_n|b_n\rangle + E|E\rangle. \quad (6)$$

We have the following coupling properties:

$$\begin{aligned} &\langle a_\omega|H|a_\omega\rangle = \omega - i\gamma_\omega, \quad \langle b_n|H|b_n\rangle = \omega_n - i\gamma_n, \\ &\langle a_\omega|H|b_n\rangle = V_n, \quad \langle a_\omega|H|E\rangle = 0, \\ &\langle E|H|b_n\rangle = f_n. \end{aligned} \quad (7)$$

We also assume regular-, chaotic states, and state of the incident beam to be orthogonal to one another [52]. We can now take the Schrödinger equation

$$H|\psi\rangle = \omega_0|\psi\rangle \quad (8)$$

and sandwich it with

(1) $\langle a_\omega|$, to obtain

$$(\omega - i\gamma_\omega)a_\omega + \sum_n b_n V_n = \omega_0 a_\omega; \quad (9)$$

(2) $\langle b_n|$, and we get

$$b_n = \frac{a_\omega V_n + f_n E}{(\omega_0 - \omega_n) + i\gamma_n}. \quad (10)$$

We now plug Eq. (10) into Eq. (9) to obtain

$$a_\omega = \frac{E \sum_n \frac{f_n V_n}{(\omega_0 - \omega_n) + i\gamma_n}}{(\omega_0 - \omega) + i\gamma_\omega - \sum_n \frac{V_n^2}{(\omega_0 - \omega_n) + i\gamma_n}}. \quad (11)$$

As before, we assume that $\omega_n \simeq \omega_0$ for all chaotic states, which simplifies Eq. (11) to the form

$$a_\omega = -\frac{E \sum_n f_n \frac{V_n}{\gamma_n}}{[\gamma_\omega + i(\omega_0 - \omega)] + \sum_n \frac{V_n^2}{\gamma_n}}. \quad (12)$$

Equation (12) differs from Eq. (5), previously derived, by an overall minus sign, which however does not affect the excitation probability (squared modulus of the amplitude), and by the ω_0-ω term, where the two frequencies are swapped with respect to Eq. (5).

C. Probability of excitation of a regular mode

Let us now rewrite

$$\sum_n f_n \frac{V_n}{\gamma_n} \simeq n_\gamma \left\langle \frac{f_n V_n}{\gamma_n} \right\rangle, \quad (13a)$$

$$\sum_n \frac{V_n^2}{\gamma_n} \simeq n_\gamma \left\langle \frac{V_n^2}{\gamma_n} \right\rangle, \quad (13b)$$

where the averages are taken over n_γ chaotic modes of small enough linewidth (γ sets the upper bound) to effectively contribute to the excitation of the regular modes. In that way, we can express Eq. (5) as

$$a_\omega = \frac{E_0 n_\gamma \left\langle \frac{f_n V_n}{\gamma_n} \right\rangle}{[\gamma_\omega + i(\omega - \omega_0)] + n_\gamma \left\langle \frac{V_n^2}{\gamma_n} \right\rangle}. \quad (14)$$

This can be rewritten (setting $\epsilon = \frac{E_0 \langle f_n V_n/\gamma_n \rangle}{\langle V_n^2/\gamma_n \rangle}$ and $\Gamma = \frac{\gamma_\omega}{\langle V_n^2/\gamma_n \rangle}$) as

$$a_\omega = \epsilon \frac{n_\gamma}{\left[\Gamma + i\frac{(\omega - \omega_0)}{\langle V_n^2/\gamma_n \rangle}\right] + n_\gamma}. \quad (15)$$

The excitation probability for the regular mode is therefore

$$|a_\omega|^2 = \epsilon^2 \frac{n_\gamma^2}{(\Gamma + n_\gamma)^2 + \frac{(\omega - \omega_0)^2}{\left\langle V_n^2/\gamma_n \right\rangle^2}}, \quad (16)$$

which becomes, at resonance [38],

$$|a_\omega|^2 = \epsilon^2 \frac{n_\gamma^2}{(\Gamma + n_\gamma)^2}. \quad (17)$$

D. Statistics of chaotic states

Equation (17) is central to our construction, as it links the number of excited regular modes (proportional to $|a_\omega|^2$), that we measure directly, to the number of chaotic modes n_γ, that we estimate as follows.

In principle, we lack information on the typical decay rate or linewidth of the chaotic modes that contribute to the excitation of the regular ones. Specifically, we do not know whether the latter decay within the Ehrenfest time $\tau_{\rm Ehr}$ of quantum-to-classical correspondence, or whether they are, on average, significantly longer lived (quasibound). Because of that, we present here three different models, the first entirely classical, the second based on the truncation of random unitary matrices [42], suitable for quasibound states, and the third that combines the previous two [43], and that thus applies to an intermediate timescale.

The following analysis refers to the classical dynamics of the chaotic billiard, and all the time-related quantities are expressed in units of the average ("Poincaré") time between two consecutive bounces of a ray on the boundary.

(1) We begin with the classical description, and assume that the motion inside the chaotic part of the phase space is hyperbolic, so that the survival probability takes the form $P(t) \propto e^{-t/\tau_d}$, where τ_d is the mean dwell time of a trajectory in the system. If there are M states in the cavity at $t = 0$, the average number of states that survive in the cavity by time $t^* < \tau_{\rm Ehr}$ is given by

$$n(t^* < \tau_{\rm Ehr}) = Me^{-t^*/\tau_d} = Me^{-1/\gamma\tau_d} \tag{18}$$

having set $\gamma = 1/t^*$. In particular, the number of states that survive at the Ehrenfest time is given by

$$n(\tau_{\rm Ehr}) = Me^{-t_{\rm Ehr}/\tau_d} = MN^{-1/\hat{\mu}\tau_d}, \tag{19}$$

where $\hat{\mu}$ is of the order of the Lyapunov exponent, N is the number of open channels, so that $\tau_d = M/N$, and we took $\tau_{\rm Ehr} = \hat{\mu}^{-1} \ln N$ (see Appendix A for details).

(2) The statistics of the spectrum of a chaotic Hamiltonian is typically determined by means of Random Matrix Theory (RMT) [53]. We now follow this approach in order to estimate the number of long-lived states, starting with an expression for the probability distribution $P(r)$, $r = e^{-\gamma_n/2}$ (γ_n escape rate of an eigenstate of the open system), obtained from truncated random matrices [42]:

$$\Phi(r) = C\frac{2r}{(1-r^2)^2}, \tag{20}$$

where C is a normalization constant. The number of eigenstates $n_{\gamma,\rm RMT}$ with escape rate $\gamma_n < \gamma$ is then evaluated from the integral of Eq. (20),

$$n_{\gamma,\rm RMT} = \int_{r_\gamma}^{\sqrt{1/\tau_d}} \Phi(r)\, dr, \tag{21}$$

with $r_\gamma = e^{-\gamma/2}$, under the assumptions that $\tau_d \gg 1$, and $\lim_{\gamma\to\infty} n_{\gamma,\rm RMT} = M - N$, that is the number of states that do not decay instantaneously. The final result is

$$n_{\gamma,\rm RMT} \simeq M\left[1 - \frac{1}{\tau_d}\frac{1}{1-e^{-\gamma}}\right]. \tag{22}$$

(3) If we then want to remove the states that decay within Ehrenfest time from the estimate of n_γ, we just combine (22) and (19), obtaining [38,43]

$$n_{\gamma,\rm Weyl} = \frac{M}{N^{1/\hat{\mu}\tau_d}}\left[1 - \frac{1}{\tau_d(1-e^{-\gamma})}\right]. \tag{23}$$

The previous expression, which scales as a nonintegral power of the number of states consistently with the fractal Weyl law [43,45], is therefore a semiclassical correction to the RMT prediction. It depends on the Lyapunov exponent of the chaotic dynamics, and therefore it takes into account system-specific properties.

In what follows, we will validate Eq. (18), Eq. (22), and Eq. (23) respectively against the experimental data.

III. CHAOTIC RAY DYNAMICS AND EXCITATION OF REGULAR MODES

A. Absorber and phase space

In order to achieve the full opening required to test the above predictions, we introduce an absorber in the cavity. In the analysis, the dielectric microcavity [Fig. 2(a), inset] has the deformed circle $\rho(\phi)$ as boundary (see Sec. IV for details), which encloses an absorber of shape $\rho(\phi) - R$. Figure 2 shows the classical phase space, together with the critical line of total internal reflection ($\sin\theta_c$), as well as the line given by the incidence angle θ_a, below which the reflected ray hits the absorber. In what follows we neglect the dependence of θ_a on ϕ by taking the average value, approximately given by the ratio r of the mean radius of the absorber to the cavity's. We assume in this model that the rays that hit the absorber are completely absorbed by it. We will justify the assumption in Sec. IV. We also previously remarked that only a subset of longer-lived chaotic states, out of those available in the whole phase space, effectively contribute to the excitation of the regular modes [Eqs. (13)]. Because of that, we do not count the rays that escape the cavity by refraction into the air with an angle of incidence $\theta \ll \theta_c$, since these are very lossy and they are not expected to contribute to the excitation of the regular modes. Instead, we only take into account the states supported on a strip of the chaotic phase space with momentum above a certain threshold, $\sin\theta > \sin\theta_{\rm th}$, to be chosen below but close enough to the critical line of total internal reflection. Let us introduce the notation $\xi \equiv \sin\theta_a - \sin\theta_{\rm th}$ to indicate the strip of the phase space opened by the absorber. The N open channels (cf. Sec. II D) out of the M Planck cells available in the phase space, are produced by the absorber (full opening, N_a) and the refraction out of the cavity (partial opening, N_r), so that the mean dwell time of a ray is given by [38]

$$\tau_d = \frac{M}{N_a + N_r} \tag{24}$$

with $N_r = \frac{M}{A}\int_{\sin\theta_a}^{\sin\theta_c} T(\sin\theta)\, d\sin\theta$, T transmission coefficient according to Fresnel law, and A area of the chaotic phase space in exam, while $N_a = M\xi/A$.

The mean dwell time plays a central role in the present study, since the main idea of our experiments resides in counting resonances as a function of the size of the absorber,

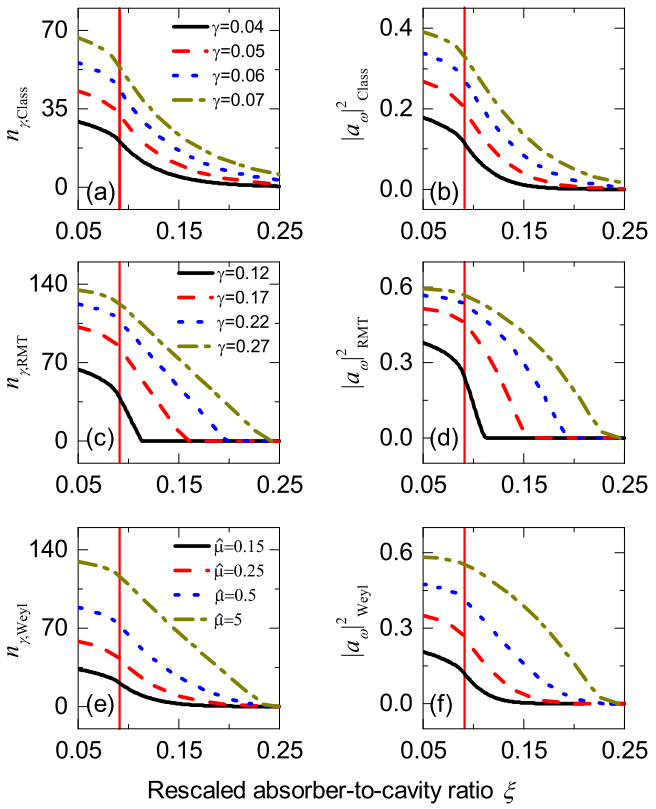

FIG. 3. (a), (c), (e) Number of chaotic states n_γ vs the rescaled absorber-to-cavity ratio ξ, obtained by classical, RMT and Weyl law respectively. (b), (d), (f) The corresponding expectations for $|a_\omega|^2$. The red vertical line corresponds to the critical angle, $\sin\theta_c \simeq 0.69$. Here $\sin\theta_{\rm th} = 0.6$. (c)–(f) adapted from Ref. [38].

and therefore in using τ_d as the variable for the predictions (18), (22), and (23).

B. Excitation of the regular modes

We proceed by steps and examine the above theories (classical, RMT, semiclassical) for the number of chaotic states n_γ with escape rate less than γ, as a function of the mean dwell time τ_d, or, equivalently, the rescaled absorber-to-cavity ratio ξ. We set $\hat{\xi} = 1/\tau_d = \xi/A + N_r/M$, and rewrite the predictions of Sec. II D in terms of $\hat{\xi}$.

(1) The classical model [Eq. (18)] becomes

$$n_{\gamma,\rm Class} = Me^{-\hat{\xi}/\gamma} \tag{25}$$

in the new notation. Figure 3(a) shows the decay of the number of states as the opening increases in size, and [Fig. 3(b)] the correspondent decay of the probability of excitation of a regular mode: while $n_{\gamma,\rm Class}$ and $|a_\omega|^2_{\rm Class}$ [obtained by plugging Eq. (25) into Eq. (17)] decrease slowly for ξ small such that $\theta_a < \theta_c$, that is when the loss is mainly due to refraction into air, both quantities fall off rapidly, and nonlinearly, when the loss is entirely due to the absorber (full opening).

(2) The RMT-based prediction, Eq. (22), is also rewritten as a function of $\hat{\xi}$ [38]:

$$n_{\gamma,\rm RMT} = M\left[1 - \frac{\hat{\xi}}{1-e^{-\gamma}}\right]. \tag{26}$$

Its behavior is illustrated in Fig. 3(c): here $n_{\gamma,\rm RMT}$ decreases linearly with ξ in the region of total internal reflection, when the loss is entirely due to the absorber. The probability of excitation of the high-Q regular modes $|a_\omega|^2_{\rm RMT}$ starts to fall off as ξ reaches some critical value, controlled by the parameter γ [Fig. 3(d)]. The other parameter $\tilde{\Gamma} = \frac{\gamma_\omega}{M\langle V_n^2/\gamma_n\rangle}$ controls the slope of the curve.

(3) The semiclassical estimate (23) becomes, as a function of $\hat{\xi}$ [38],

$$n_{\gamma,\rm Weyl} = \frac{M^{1-\hat{\xi}/\hat{\mu}}}{\hat{\xi}^{\hat{\xi}/\hat{\mu}}}\left[1 - \frac{\hat{\xi}}{1-e^{-\gamma}}\right]. \tag{27}$$

The rescaled Lyapunov exponent $\hat{\mu}$ of the chaotic region of the phase space is what really characterizes (27), which resembles the linear RMT expression (26) for large enough $\hat{\mu}$, and otherwise becomes visibly nonlinear [Figs. 3(e)] when $\hat{\mu} \ll 1$. This nonlinearity produces a characteristic tail in the probability $|a_\omega|^2_{\rm Weyl}$ [Fig. 3(f)], similar to that of the classical prediction (18). We therefore interpret it as a signature of chaos, which is most evident slightly above the onset of chaotic dynamics.

C. Transient chaos

The survival probability leading to Eqs. (18) and (23) for the classical estimates of the number of decaying states, has an exponential form because it rests on the assumption of a fully chaotic phase space. However, the phase portraits of Fig. 2 suggest the presence of nonhyperbolic ("sticky") regions [54,55], as well as of partial transport barriers [56,57] even in the chaotic part of the phase space, which would make the survival probability decay algebraically, instead of exponentially. We address the issue by performing extensive ray-dynamics simulations of the microcavity-shaped billiard of two different deformation factors, and computing the survival probability in the chaotic region. Here the absorber at the center of the billiard constitutes the sole, full opening. Figure 4 illustrates the results: despite an overall power-law decay, a closer look at the short-time dynamics reveals that the decay is initially exponential, behavior known as transient chaos [58]. The applicability of a model involving fully developed chaos would depend on how the Ehrenfest time of quantum-to-classical correspondence compares to the typical transition time $\tau_{\rm trans}$ by which the chaotic decay turns algebraic. We estimated $\tau_{\rm trans} = 6(14)$ units of Poincaré time for a cavity with deformation factor $\eta = 11.7\%(4.2\%)$. We shall estimate the Ehrenfest times of the microcavity of these deformations in Sec. V A, and confirm the validity of the fully chaotic model for the present experiments.

IV. EXPERIMENTAL SETUP AND MEASUREMENT

The experimental apparatus consists of a deformed toroidal microcavity of boundary shape given by the curve

$$\rho(\phi) = \begin{cases} \rho_0\left(1 + \epsilon\sum_{i=2,3} a_i\cos^i\phi\right) & \text{for } \cos\phi \geqslant 0, \\ \rho_0\left(1 + \epsilon\sum_{i=2,3} b_i\cos^i\phi\right) & \text{for } \cos\phi < 0, \end{cases} \tag{28}$$

with $\rho_0 = 60\,\mu$m, $a_2 = -0.1329$, $a_3 = 0.0948$, $b_2 = -0.0642$, and $b_3 = -0.0224$. The WGMs in the deformed

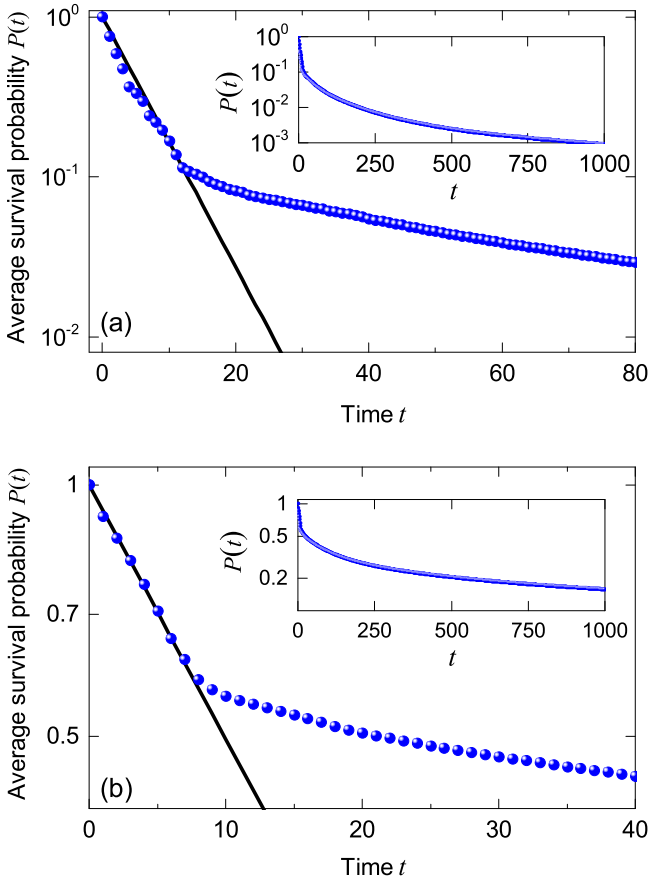

FIG. 4. Survival probability in the chaotic region (log scale). Points: average survival probability $P(t)$ of a ray in the microcavity vs t (in units of Poincaré time) at: (a) $\eta = 11.7\%$, $\xi = 0.13$, from 10^6 randomly started trajectories. Line: $P(t) \propto \exp(-t/\tau_d)$, $\tau_d = 6$ (from Ref. [38]); (b) $\eta = 4.2\%$,$\xi = 0.1$, $\tau_d = 14$. Insets: the long-time simulation showing algebraic decay.

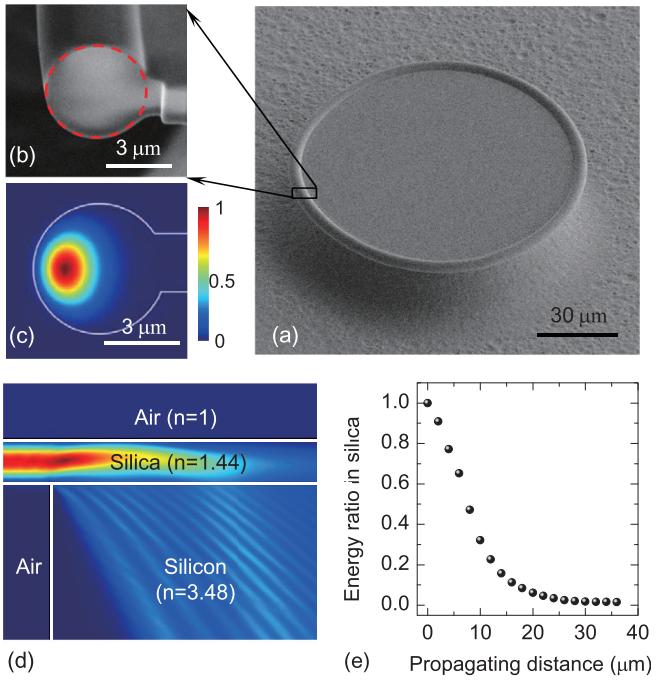

FIG. 5. (a) Image of the microcavity obtained by scanning electron microscopy (SEM). (b) SEM cross-section image of the toroidal part, taken at an angle of 56° with the horizontal direction. (c) Finite-element method simulation of a fundamental TE mode (color scale in arbitrary units). The white solid curve is the boundary of the cavity. (d) Finite-element method simulation of the light propagating inside the 2-μm-thick silica waveguide bonding with a thick silicon layer (color scale in arbitrary units). (e) Fraction of remaining energy in silica vs the propagating distance.

microcavity have been demonstrated to possess ultrahigh quality factors in excess of 10^8 in the 1550 nm wavelength band and to exhibit highly directional emission towards the 180° far-field direction, which emits tangentially along the cavity boundaries at polar angles $\phi = \pi/2$ and $\phi = 3\pi/2$ [20]. The deformation is controlled by $\eta = (d_{\max} - d_{\min})/d_{\max}$, $d_{\max}$ and $d_{\min}$ respectively the maximum and minimum diameters of the cavity. The parameter η is related to ϵ through $\eta = \epsilon|a_2 + a_3 + b_2 - b_3|/2$. The microcavity is coupled to a free-space propagating laser beam of wavelength $\lambda \simeq 1550$ nm (swept from 1555 nm to 1545 nm, free-spectral range 4.4 nm [59]), or 635 nm (swept from 639 nm to 637 nm, free-spectral range 0.74 nm), as shown in Fig. 1. The microtoroid [refractive index $\simeq 1.44, 1.46$ depending on λ, Fig. 5(a)] has principal or minor diameters of 120/5 μm, consistently with the two-dimensional model. Thus the effective Planck constant $h_{\text{eff}} \sim \lambda/a \sim 10^{-2}$ (a: principal diameter) justifies the semiclassical analysis. The microcavity is fabricated through optical lithography, buffered HF wet etching, XeF_2 gas etching, and CO_2 pulse laser irradiation. The resulting silica microtoroid is supported by a silicon pillar of similar shape, which has a high refractive index ($\simeq$3.48,3.88), and it acts as the absorber in the model.

After each measurement of the transmission spectrum (Fig. 6), the top diameter of the silicon pillar, connected with the silica disk, is progressively reduced by a new isotropic XeF_2 dry etching process. In this way we control the openness of the microcavity with the ratio r between the top diameters of pillar and toroid. Finite-element method simulations [Figs. 5(d) and 5(e)] show that the light power decreases to less than 5% of the input value, when propagating by a distance of 20 μm inside the 2-μm-thick silica waveguide bonding with a silicon wafer, as it is reasonable to expect, given the high refractive index of the silicon. Thus the silicon pillar acts as a full absorber, consistently with the model presented here. On the other hand, high-Q regular modes living inside the toroidal part, whose circular cross section has diameter of 5 μm, do not leak into the silicon pillar and therefore are not directly affected by the pillar size. Figure 5(c) illustrates the numerical simulation of a regular TE mode, that is confined in the toroidal region. Due to the free-space propagation, the laser beam can only enter the cavity with a relatively large angle of incidence, which results in smaller angles of refraction into the resonator, and of incidence with its boundary at the next collisions. As a consequence, the laser beam only directly excites the chaotic cavity modes localized in the central region of the cavity, which in turn couple with the regular modes localized in the outer toroid via dynamical tunneling, consistently with the model of Sec. II.

The dependence of the transmission spectra on the pillar size is shown in Fig. 6. When the pillar approaches the inner

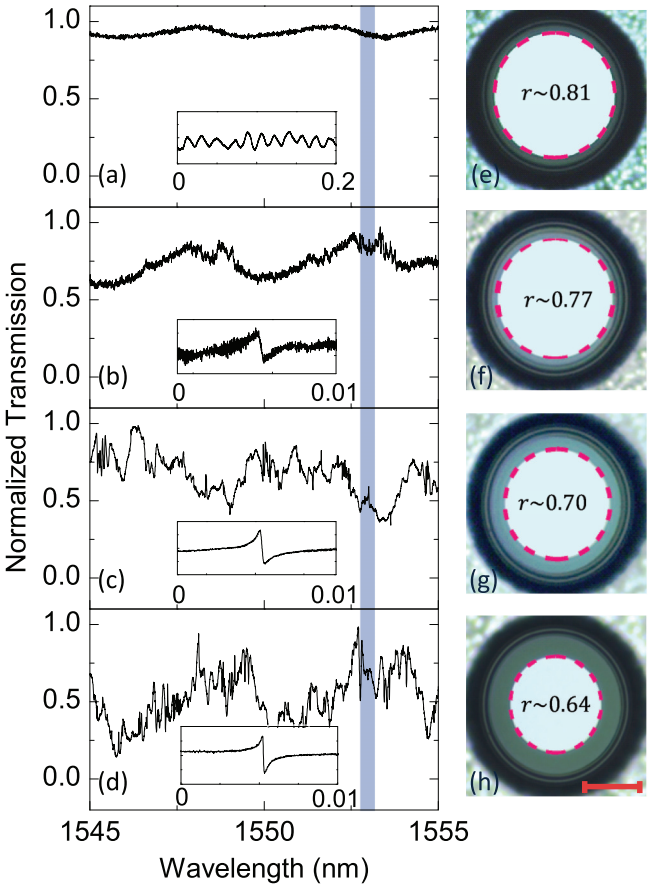

FIG. 6. Normalized transmission and top-view optical images of the cavity with $r \simeq 0.81$ [(a) and (e)], 0.77 [(b) and (f)], 0.70 [(c) and (g)], 0.64 [(d) and (h)]. Inset of (a) shows background noise. Insets of (b)–(d) show the high-Q modes. Reflection of the silica-to-silicon interface results in a brighter color for the silicon pillar in the optical image (boundary shown by red dashed curves). Scale bar is 50 μm. Adapted from Ref. [38].

edge of the toroid [Figs. 6(a) and 6(e), $r \simeq 0.81$], no high-Q regular modes are observed in the spectrum, since most of the probe laser field in the cavity radiates into the silicon and cannot tunnel to couple with high-Q regular modes. As we gradually reduce the size of the pillar [Fig. 6(f), $r \simeq 0.77$], increasingly many high-Q modes appear in the spectrum [Fig. 6(b)]. When the absorber-to-cavity ratio r is small enough [Figs. 6(g) and 6(h), $r \lesssim 0.7$], the transmission no longer changes sensibly [Figs. 6(c) and 6(d)], and the number of high-Q modes in the spectrum also stabilizes.

It is noted that the high-Q regular modes are easily recognized even when the coupling efficiency is low, because linewidths coming from noise are typically orders of magnitude wider than those of the high-Q resonances in the transmission spectrum, as shown in the insets of [Fig. 6(a) and 6(b)]. That is to say, nearly all the existing high-Q modes are conspicuous in the spectra and can be detected.

V. STATISTICS OF CHAOTIC RESONANCES

As anticipated, we use the transmission spectra to test the theory, by counting the excited high-Q regular modes for different sizes of the silicon pillar. A polarization controller is used to alternatively excite TE or TM modes, which are collected by the photon receiver, and read from the transmission spectra. We single out and add up the modes with high Q factors ($Q > 10^5$) for both polarizations, and then multiply the result by the ratio of free-spectral range to the range of wavelengths swept by the laser beam [for example, that is 0.74/(639–637) for visible light]. Since TE and TM modes are not perfectly orthogonal to each other in the real microcavity, some may be counted twice, which is the main source of uncertainty in our data.

TABLE I. Parameters related to the best-fit of Eqs. (25) and (29) to the data, and to the experimental conditions. Here γ is expressed in units of T^{-1}, with $T \simeq 3 \times 10^{-13}$ s Poincaré time.

$\tilde{\Gamma}$	γ	η	λ (nm)	M	χ^2
6×10^{-5}	0.01	4.2%	630	40	4
2×10^{-4}	0.015	4.2%	1550	20	1.6
6×10^{-4}	0.014	6.0%	630	40	3.1
10^{-3}	0.017	6.0%	1550	20	1.1
2.4×10^{-4}	0.017	11.7%	1550	50	0.4

Based on the assumption (discussed in Sec. VI) that the number of regular modes excited via dynamical tunneling is proportional to the probability of excitation of a single regular mode, given by Eq. (17), we henceforth test all the predictions presented in the theoretical sections, and plug Eqs. (25), Eq. (22), and Eq. (23) respectively into the expectation

$$n_{\rm reg} = \kappa \frac{n_\gamma^2}{(\Gamma + n_\gamma)^2} \tag{29}$$

for the counted high-Q resonances.

A. Classical model

We start with the classical model. Equation (25) is plugged into Eq. (29) and fitted to the data via the parameters $\tilde{\Gamma}$, γ, up to an overall multiplicative constant. The total number of chaotic states is estimated theoretically as $M \simeq A/h_{\rm eff}$ (A area of the chaotic phase space we consider). The results are shown in Fig. 7, with details in Table I. The classical prediction

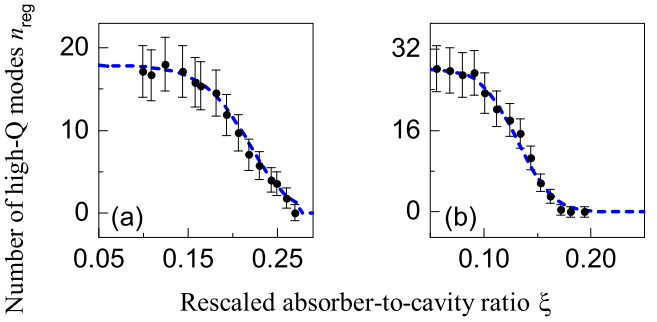

FIG. 7. Dots: number of high-Q regular modes (n_ω) observed in the transmission spectra of the microcavity coupled to infrared light, as a function of rescaled absorber-to-cavity ratio ξ. Blue dashed curve: best fit of the classical prediction (25) [together with Eq. (29)]. Left: $\eta = 11.7\%$; right: $\eta = 6\%$. Here $\sin\theta_c \simeq 0.69$ and $\sin\theta_{\rm th} = 0.6$.

TABLE II. Lower and upper bounds for the typical Ehrenfest time (in units of Poincaré time) of the chaotic states of microcavities with different deformation factors, coupled to either infrared or visible light, in comparison with the average $\gamma_{\rm Class}^{-1}$ coming from Table I, and $\gamma_{\rm Weyl}^{-1}$ coming from Table IV.

η	λ (nm)	$\tau_{\rm Ehr}^{\rm min}$	$\tau_{\rm Ehr}^{\rm max}$	$\gamma_{\rm Class}^{-1}$	$\gamma_{\rm Weyl}^{-1}$
4.2, 6%	630	6.5	14	83	7.4
4.2, 6%	1550	15	25	63	6.3
11.7%	1550	10	14	59	5.3

appears to fit the data rather well, overall. The statistical test of χ^2 [60] evaluates the average discrepancy between expectations $[n_{\gamma,\rm Class}(\xi_i)]$ and observations $(n_{\gamma,i})$, divided by the experimental errors σ_i, in d degrees of freedom:

$$\chi^2 = \frac{1}{d}\sum_i \frac{[n_{\gamma,i} - n_{\gamma,\rm Class}(\xi_i)]^2}{\sigma_i^2}. \tag{30}$$

Here we generally obtain $\chi^2 \approx 1$, indicating that the extent of the match between observations and estimates is in accord with the error variance. However, in order for this model to be accurate, all the chaotic states indirectly detected by the experiment should decay within Ehrenfest time, which seems unlikely, in principle. The minimum decay time of the chaotic modes is determined from the best fits as γ^{-1}, and it can be compared with the Ehrenfest time (we should find $\tau_{\rm Ehr} > \gamma^{-1}$), with the latter estimated in terms of the laser wavelength, the dimensions of the cavity, the Lyapunov exponent of the classical dynamics, and the size of the absorber (see Appendix B for details). In this regard, the absorber-to-cavity ratio ξ varies within a certain range, thus we estimate upper and lower bounds for $\tau_{\rm Ehr}$ in units of the Poincaré time T, as summarized in Table II, for cavities of different deformations, coupled to either visible or infrared light. As we can see, the estimated Ehrenfest time of the rays in the microcavity is always significantly shorter than the minimal escape time γ^{-1}, although of the same order of magnitude. That suggests that the classical model for the statistics of the chaotic states alone does not describe the experiment consistently with the assumptions.

B. RMT and semiclassical predictions

Next, we validate (1) the RMT-based prediction (26), and (2) the semiclassical expression (27), which we alternatively plug into Eq. (29). The results are illustrated in Fig. 8 (details in Tables III and IV), for two microcavities of distinct deformations, probed at visible and infrared wavelengths.

In the RMT-based approach we have two fitting parameters, γ and $\tilde{\Gamma}$. Figure 8 shows overall agreement between the experimental data and this theory, particularly in the infrared band and at large deformation. However, the purely RMT model fails to capture the tail of the data at larger sizes of the absorber in the experiments with visible light, where the χ^2 significantly exceeds the optimal value of unity.

After that, the semiclassical correction (27) is tested, using the finite time Lyapunov exponent $\hat{\mu}$ evaluated by direct iteration, over a short enough time for the dynamics to be still hyperbolic (cf. Sec. III C). In addition, we still have the estimated parameter M and the fitted parameters γ and Γ. This expression is found in better agreement with the experimental data ($\chi^2 \approx 1$) than the RMT-based estimate at smaller deformation and in the visible light band, where the two predictions differ the most due to the smaller $\hat{\mu}$ (cf. Fig. 3). Specifically, the semiclassical theory accounts for the tail of the curve, that corresponds to the microcavity having the largest openings and thus with the maximum number of instantaneous decay states, where the semiclassical correction is important.

Similarly to the classical model, we check whether the fitted values of the parameter γ for the RMT and semiclassical expressions make physical sense. It is found that, typically, $\gamma \simeq 0.15$; now recall that $\gamma^{-1} = \tau_{\rm esc}$ the minimum escape time of the chaotic rays contributing to the excitation of the regular modes, from which $Q = 2\pi\nu\tau_{\rm esc} \sim 10^3$, on average ($\nu$ is the frequency of the laser beam). We find this estimate consistent with the typical order of Q independently obtained from ray-dynamics simulations (Fig. 9), which corroborates the result from the analysis. By the same token, one can write the linewidth of a resonance as $\mathrm{Im}\,\Omega = -\frac{a}{2c}\gamma$, where again a is the cavity radius and c the speed of light inside the silica. We estimate on average $\mathrm{Im}\,\Omega \simeq -0.1$, which is close to the median value $\mathrm{Im}\,\hat{\Omega} \simeq -0.15$ of the distribution of resonances found in the numerical experiment of Ref. [32], where a stadium-shaped microcavity of refractive index $n = 1.5$ was considered. At last, but importantly, we compare γ^{-1} with the Ehrenfest time. Equations (26) and (27) are based on the assumption $\tau_{\rm Ehr} < \gamma^{-1}$, the opposite of the classical model's. We find from our fits (Tables III and IV) that $\tau_{\rm Ehr} \approx \gamma^{-1}$ in all the realizations of the experiments, and therefore the above assumption is not always validated within the uncertainties. We believe at the present stage the semiclassical prediction to be a more accurate model for the statistics of the chaotic states than the entirely classical one. All the same, a number of chaotic states that escape within Ehrenfest time may also contribute to the excitation of the regular modes, for our experiment to capture that intermediate time scale at the border line between ray- and purely wavelike modes. One could at that point combine theories using the following expression [61]:

$$n_\gamma = \varepsilon n_{\gamma,\rm Class} + (1-\varepsilon) n_{\gamma,\rm Weyl}, \tag{31}$$

which would, however, add one presently unknown parameter (ε) to the analysis.

VI. TUNNELING RATES AND STATISTICS OF LINEWIDTHS

In this section, we discuss the proportionality between the probability of excitation of a single regular mode and the number of excited regular modes in the microcavity, which we have estimated as

$$n_{\rm reg} = \kappa \frac{n_\gamma^2}{(\Gamma + n_\gamma)^2}. \tag{29}$$

In doing so, we have implicitly neglected the ω dependence of the excitation probability of a regular mode at resonance

$$|a_\omega|^2 = \epsilon^2 \frac{n_\gamma^2}{(\Gamma + n_\gamma)^2}. \tag{17}$$

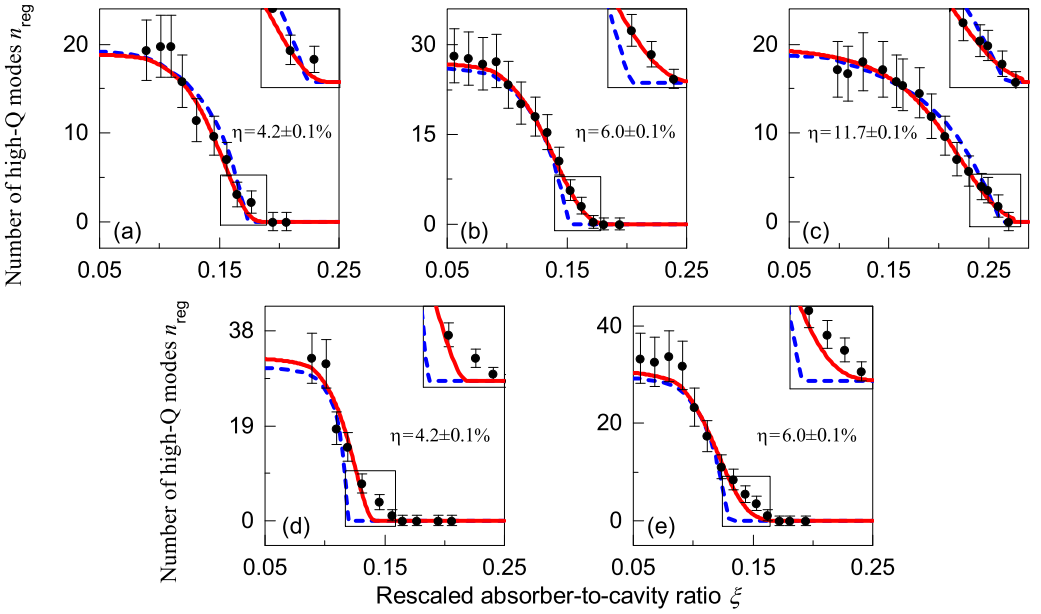

FIG. 8. Number of high-Q regular modes ($n_{\rm reg}$) observed in the transmission spectra of the microcavity (dots), as a function of rescaled absorber-to-cavity ratio ξ. Blue dashed and red solid curves are respectively RMT- and semiclassical prediction best fits. (a), (b), (c) Infrared light; (d), (e) visible light. Here $\sin\theta_c \simeq 0.69$ and $\sin\theta_{\rm th} = 0.6$. Insets: the area where the two curves differ most.

In order to better understand this approximation, let us restart from the excitation amplitude

$$a_\omega = \frac{E_0 \sum_n f_n \frac{V_n}{\gamma_n}}{[\gamma_\omega + i(\omega-\omega_0)] + \sum_n \frac{V_n^2}{\gamma_n}}. \tag{5}$$

Here, we can regard the term

$$\gamma_\omega^{\rm tot} = \gamma_\omega + \sum_n \frac{V_n^2}{\gamma_n} \tag{32}$$

as the total (hence measured) linewidth [47], where the first term γ_ω indicates the intrinsic linewidth of the regular mode, while the second, $\gamma_\omega^{\rm dyn} \equiv \sum_n \frac{V_n^2}{\gamma_n}$, represents the decay rate into the chaotic modes. It is to be determined whether the fluctuations ultimately due to the dependence of these quantities on the frequency ω of the mode can be neglected, say, to a first-order approximation.

In what follows, we first argue that such fluctuations are small compared to the decay rates and therefore the linewidths of the regular modes, based on a semiclassical treatment of dynamical tunneling, and secondly we test the validity of the approximation (29) with two independent experiments.

A. Action-based prediction of tunneling rates

The tunneling rates into the chaotic field of distinct regular WGMs localized in the toroid of the microresonator, or equivalently, in the top region of the phase portraits of Fig. 2, vary with the momentum of the corresponding rays, as it can be inferred from the expression for the penetration through a potential barrier [62]

$$\gamma^{\rm tun} \propto e^{-\frac{2}{\hbar}\int_a^b |p|\,dq}. \tag{33}$$

Intuitively, since the WGMs are confined in a narrow strip of the phase space (cf. Fig. 2), the distributions of momenta of the regular trajectories and of their tunneling rates into the chaotic sea are also supposedly quite narrow. For an estimate of the variation of the tunneling rate of a regular mode with the momentum, we need to be more accurate, and we may use an expression derived in Ref. [63] for the tunneling rate out of a stability island into the chaotic region of a mixed phase space

$$\gamma_\omega^{\rm dyn} = \frac{c}{\sqrt{1-S_\omega}} e^{-\frac{2A_{\rm reg}}{h_{\rm eff}}\{\sqrt{1-S_\omega} - S_\omega \ln(\frac{1+\sqrt{1-S_\omega}}{\sqrt{S_\omega}})\}}, \tag{34}$$

where c is a constant, while $S_\omega = A_{\rm reg}^{-1} \oint p dq$ is the quantized action of the classical orbit corresponding to the regular mode

TABLE III. Parameters related to the best fit of Eqs. (26) and (29) to the data and to the experimental conditions in Fig. 8. Here γ is expressed in units of T^{-1}, with $T \simeq 3 \times 10^{-13}$ s Poincaré time.

Γ	γ	η	λ(nm)	M	χ^2
0.025	0.1	4.2%	630	40	16
0.08	0.15	4.2%	1550	20	3.2
0.07	0.11	6.0%	630	40	11
0.08	0.13	6.0%	1550	20	2
0.11	0.17	11.7%	1550	50	1.1

TABLE IV. Parameters related to the best-fit of Eqs. (27) and (29) to the data, and to the experimental conditions in Fig. 8. Here γ and μ are expressed in units of T^{-1}, with $T \simeq 3 \times 10^{-13}$ s Poincaré time.

Γ	γ	η	λ (nm)	M	μ	χ^2
0.24	0.12	4.2%	630	40	0.05	6.9
0.28	0.16	4.2%	1550	20	0.05	1.5
0.55	0.15	6.0%	630	40	0.05	4.8
0.54	0.16	6.0%	1550	20	0.05	0.6
0.73	0.19	11.7%	1550	50	0.1	0.5

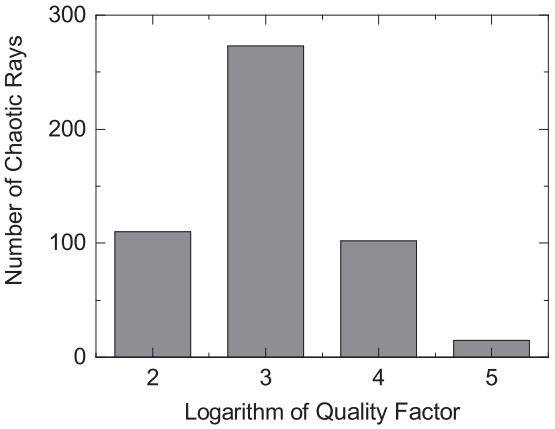

FIG. 9. Statistics of the quality factor for the chaotic rays in the deformed microcavity, from a ray-dynamics simulation.

in exam, scaled by the area of the regular region of the phase space $A_{\rm reg}$. In the present construction $S_\omega < 1$, which is also true in our setting. Then, by Taylor-expanding the action, the overall expression for the tunneling rate becomes

$$\gamma_\omega^{\rm dyn} \approx c e^{-\frac{2A_{\rm reg}}{h_{\rm eff}}\{1+\frac{S_\omega}{2}\ln S_\omega\}}. \tag{35}$$

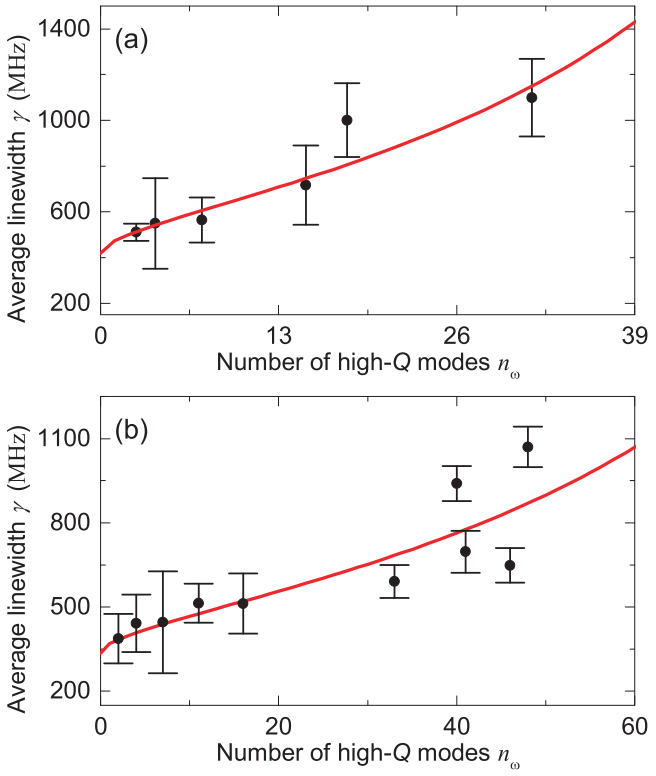

FIG. 10. Dots: average linewidth of the excited regular modes vs. their number from a free-space coupling experiment (cf. Fig. 6). Each data point represents one experiment with a different size of the silicon pillar. Solid line: best-fit curve of Eq. (41). (a) $\eta = 4.2\%$, $\lambda = 635$ nm, with fitting parameters $\gamma_{\rm reg} = 419$ MHz, and $\kappa = 78$. (b) $\eta = 6\%$, $\lambda = 635$ nm, $\gamma_{\rm reg} = 378$ MHz, and $\kappa = 120.5$.

At this point, one can compute with some algebra the differential

$$d\gamma_\omega^{\rm dyn} \approx -\gamma_\omega^{\rm dyn}\frac{A_{\rm reg}}{h_{\rm eff}}\ln S_\omega\, dS_\omega, \tag{36}$$

and thus an estimate for the relative error of the tunneling rate with the change in action

$$\frac{\Delta\gamma_\omega^{\rm dyn}}{\gamma_\omega^{\rm dyn}} \approx -\frac{A_{\rm reg}}{h_{\rm eff}}\ln S_\omega \Delta S_\omega. \tag{37}$$

Recalling the definition of action, and, in particular, that the WGMs in the microcavity are supported on regular orbits in the upper part of the phase space that closely follow the boundary, where the momentum p is almost constant along each trajectory, we may write the change in action as

$$\Delta S_\omega \simeq \frac{2\pi\,\Delta p}{A_{\rm reg}}, \tag{38}$$

whence the estimate $\frac{\Delta\gamma_\omega^{\rm dyn}}{\gamma_\omega^{\rm dyn}} \sim 10^{-1}$ in our experimental conditions.

B. Statistics of the regular modes and their linewidths

The expression

$$\gamma_\omega^{\rm tot} = \gamma_\omega + \sum_n \frac{V_n^2}{\gamma_n} \simeq \gamma_{\rm reg} + n_\gamma\left\langle\frac{V_n^2}{\gamma_n}\right\rangle \tag{39}$$

indicates that $\gamma_\omega^{\rm tot}$ increases with n_γ. We shall now neglect the dependence on ω, and derive an expression for $\gamma_{\rm reg}^{\rm tot}$ in terms of the number of regular modes $n_{\rm reg}$, to be tested with an experiment. Let us first write n_γ as a function of the observed quantity $n_{\rm reg}$, by solving the quadratic equation (29)

$$n_\gamma = \Gamma\frac{n_{\rm reg} + \sqrt{\kappa n_{\rm reg}}}{\kappa - n_{\rm reg}}. \tag{40}$$

Recalling the definition $\Gamma = \frac{\gamma_\omega}{\langle V_n^2/\gamma_n\rangle}$, we have

$$\gamma_{\rm reg}^{\rm tot} = \gamma_{\rm reg}\left[1 + \frac{n_{\rm reg} + \sqrt{\kappa n_{\rm reg}}}{\kappa - n_{\rm reg}}\right]. \tag{41}$$

We may now fit this prediction to the data in the free-space coupling experiment, that is the number of detected high-Q modes, and their linewidths. Figure 10 shows that the data points representing the average linewidths of the regular modes do follow the trend predicted by Eq. (41).

Although the fluctuations can be significant here [Fig. 10(b)], overall quantitative consistency between the proposed model and the data is definitively found through an auxiliary experiment, illustrated in Figs. 11(a) and 11(b), and described as follows. The WGMs are excited directly (no excitation of chaotic modes) through a tapered fiber [64]. The silicon pillar attached to the microtoroid has largest size, so that dynamical tunneling is inhibited and no whispering-gallery mode can be excited with the free-space coupling [Fig. 11(c)]. Measuring linewidths of the detected modes results in a quality factor $Q_{\rm reg}$ typically of the order of 10^6–10^7.

We now compare this value with the average fitting parameter $\gamma_{\rm reg} = 399$ MHz of Eq. (41) to the data of Fig. 10, which is related to the average intrinsic $Q_{\rm reg}$ factor of the

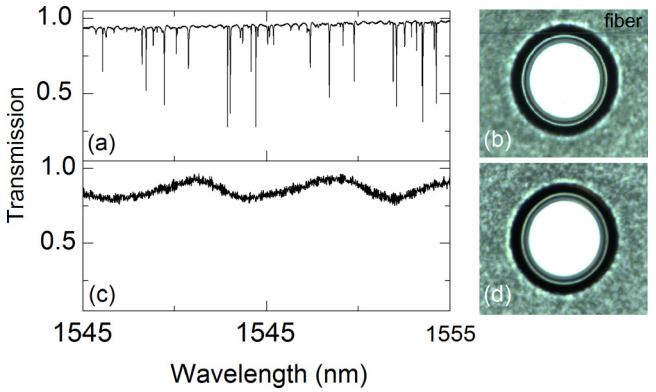

FIG. 11. Normalized transmission and top-view images of the cavity coupled by fiber taper [(a) and (b); notice the fiber beside the cavity] and free-space laser beam [(c) and (d)]. The resonances in (a) have Q factors typically of the order of 10^6–10^7. Here the absorber-to-cavity ratio is $r \simeq 0.83$.

WGMs as $Q_{\rm reg} = 2\pi\nu/\gamma_{\rm reg} \simeq 5 \times 10^6$, consistently with the outcome of the fiber-taper experiment.

Thus, the overall enlargement of the average linewidths with the number of observed regular modes supports the approximations leading to Eq. (29).

VII. CONCLUSION AND DISCUSSION

We count statistics of chaotic resonances in a deformed optical microcavity by the sole experimental detection of high-Q regular modes, using the coupling between regular and chaotic modes, which occurs via dynamical tunneling.

Being a priori unaware of the typical escape time of the chaotic modes that effectively contribute to the excitation of the regular modes, we use the experimental data to validate: (1) an entirely classical model, (2) a RMT-based, purely statistical prediction, which is independent of system-specific properties, and, finally, (3) a semiclassical correction to (2), which does depend on the Lyapunov exponent of the chaotic dynamics. We find theory (3) in the best agreement with the observations, particularly when a microcavity of lower deformation factors is coupled with visible light, while prediction (2) also proves adequate when working in the infrared.

The estimation of the Ehrenfest time of quantum-to-classical correspondence from the experimental parameters plays a key role in framing the time scale of the decay (or typical linewidth) of the chaotic states (resonances). The fastest escape occurs around Ehrenfest time, and generally within the average time of transition of the decay of correlations from exponential to algebraic, so that the classical description of the dynamics as fully chaotic seems appropriate.

On the other hand, accounting for the long-lived chaotic resonances does not seem to be as straightforward. Specifically, the effects of partial transport barriers, as well as the "stickiness" along KAM tori and stability islands are relegated to the fitting parameters in the current model. The correct detection and modeling of long-lived resonances are therefore primary issues to be addressed by future work, especially in perspective of a test of fractal Weyl law at optical frequencies. Other challenges include the possibility of estimating and measuring the amplitude of the regular-to-chaotic mode coupling, as well as developing a more refined prediction for the excitation of the regular modes.

ACKNOWLEDGMENTS

This project was supported by the National Key R&D Program of China (Grants No. 2016YFA0301302, No. 2013CB921904, and No. 2013CB328704) and the NSFC (Grants No. 61435001, No. 11654003, and No. 11474011).

APPENDIX A: RESCALING THE LYAPUNOV EXPONENT

The classical estimate of the prefactor $MN^{-1/\hat{\mu}\tau_d}$ involves Ehrenfest time, defined for *open* systems as [46]

$$\tau_{\rm Ehr} = \frac{1}{\mu}\log\frac{\tau_H}{\tau_d}. \tag{A1}$$

Here μ is the Lyapunov exponent of the closed system, τ_d is the mean dwell time, while τ_H is the Heisenberg time

$$\tau_H = \frac{h}{\Delta E}, \tag{A2}$$

with ΔE mean level spacing, that is average distance (difference) bewteen consecutive energy levels. We know, on the other hand, that $E = h\nu$, and we may therefore express Heisenberg time in terms of the frequency spacing

$$\tau_H = \frac{1}{\Delta\nu} \tag{A3}$$

and Ehrenfest time as

$$\tau_{\rm Ehr} = \frac{1}{\mu}\log\frac{N}{\Delta\Upsilon}. \tag{A4}$$

Here N is the number of open channels as we know, whereas $\Delta\Upsilon = MT\Delta\nu$, that is the mean frequency spacing times the Poincaré time (to make it dimensionless), times the number of states M. In plain words, $\Delta\Upsilon$ is the frequency range of our modes in units of the Poincaré time. At this point we can still write

$$\tau_{\rm Ehr} = \frac{1}{\hat{\mu}}\log N \tag{A5}$$

as in Sec. II D, provided that

$$\hat{\mu} = \frac{\log N}{\log N - \log\Delta\Upsilon}\mu. \tag{A6}$$

Thus we have determined the rescaling to the Lyapunov exponent, following the definition of the Ehrenfest time.

APPENDIX B: ESTIMATION OF EHRENFEST TIME

Let us start from the definition of the Ehrenfest time

$$\tau_{\rm Ehr} = \frac{1}{\mu}\ln\frac{\tau_H}{\tau_d}, \tag{B1}$$

with

$$\tau_H = \frac{h}{\Delta E} = \frac{1}{\Delta\nu}, \tag{B2}$$

$$\tau_d = \frac{M}{N}T, \tag{B3}$$

and T is the Poincaré time. For visible light, we observe about 100 WGMs in a range of wavelengths of about 10 nm, hence an estimated mean spacing between consecutive regular modes $\Delta\lambda \sim 10^{-10}$. Then

$$\Delta\nu \simeq \frac{c\Delta\lambda}{\lambda^2} \sim \frac{2\times 10^8 \times 10^{-10}}{6^2 \times 10^{-14}} = 5\times 10^{10}\ \text{Hz}, \tag{B4}$$

while

$$T \simeq \frac{a}{2c} \sim \frac{6\times 10^5}{2\times 10^8} = 3\times 10^{-13}\ \text{s}, \tag{B5}$$

with a principal diameter of the microcavity. In that way,

$$\tau_{\text{Ehr}} = \frac{1}{\mu}\ln\frac{\xi}{\Delta\nu A T}, \tag{B6}$$

where we took $\xi \simeq \frac{A}{\tau_d}$ (neglecting refraction into air), and $A = 2\pi(\sin\theta_{\max} - \sin\theta_{\text{th}})$, area of the phase space available to chaotic states above $\sin\theta_{\text{th}}$.

[1] S. L. McCall, A. F. J. Levi, R. E. Slusher, S. J. Pearton, and R. A. Logan, Whispering-gallery mode microdisk lasers, Appl. Phys. Lett. **60**, 289 (1992).

[2] K. J. Vahala, Optical microcavities, Nature (London) **424**, 839 (2003).

[3] A. B. Matsko and V. S. Ilchenko, Optical resonators with whispering gallery modes I: Basics, IEEE J. Sel. Top. Quantum Electron **12**, 3 (2006).

[4] H. Cao and J. Wiersig, Dielectric microcavities: Model systems for wave chaos and non-Hermitian physics, Rev. Mod. Phys. **87**, 61 (2015).

[5] L. Shao, X.-F. Jiang, X.-C. Yu, B.-B. Li, W. R. Clements, F. Vollmer, W. Wang, Y.- F Xiao, and Q. Gong, Detection of single nanoparticles and lentiviruses using microcavity resonance broadening, Adv. Mater. **25**, 5616 (2013).

[6] Y.-S. Park and H. Wang, Resolved-sideband and cryogenic cooling of an optomechanical resonator, Nature Phys. **5**, 489 (2009).

[7] J. U. Nöckel and A. D. Stone, Ray and wave chaos in asymmetric resonant optical cavities, Nature (London) **385**, 45 (1997).

[8] C. Gmachl, F. Capasso, E. E. Narimanov, J. U. Nöckel, A. D. Stone, J. Faist, D. L. Sivco, and A. Y. Cho, High-power directional emission from microlasers with chaotic resonators, Science **280**, 1556 (1998).

[9] J. Wiersig and M. Hentschel, Combining Directional Light Output and Ultralow Loss in Deformed Microdisks, Phys. Rev. Lett. **100**, 033901 (2008).

[10] S. Shinohara, T. Harayama, T. Fukushima, M. Hentschel, T. Sasaki, and E. E. Narimanov, Chaos-Assisted Directional Light Emission from Microcavity Lasers, Phys. Rev. Lett. **104**, 163902 (2010).

[11] Q. H. Song, L. Ge, A. D. Stone, H. Cao, J. Wiersig, J.-B. Shim, J. Unterhinninghofen, W. Fang, and G. S. Solomon, Directional Laser Emission from a Wavelength-Scale Chaotic Microcavity, Phys. Rev. Lett. **105**, 103902 (2010).

[12] Q. H. Song, L. Ge, B. Redsding, and H. Cao, Channeling Chaotic Rays into Waveguides for Efficient Collection of Microcavity Emission, Phys. Rev. Lett. **108**, 243902 (2012).

[13] X.-F. Jiang, Y.-F. Xiao, C.-L. Zou, L. He, C.-H. Dong, B.-B. Li, Y. Li, F.-W. Sun, L. Yang, and Q. Gong, Highly unidirectional emission and ultralow-threshold lasing from on-chip ultrahigh-Q microcavities, Adv. Mater. **24**, OP260 (2012).

[14] J. Ward and O. Benson, WGM microresonators: Sensing, lasing and fundamental optics with microspheres, Laser Photonics Rev. **5**, 553 (2011).

[15] S. Sunada and T. Harayama, Design of resonant microcavities: Application to optical gyroscopes, Opt. Express **15**, 16245 (2007).

[16] J. Wiersig, Formation of Long-Lived, Scarlike Modes Near Avoided Resonance Crossings in Optical Microcavities, Phys. Rev. Lett. **97**, 253901 (2006).

[17] J. Anderasen, H. Cao, J. Wiersig, and A. E. Motter, Marginally Unstable Periodic Orbits in Semiclassical Mushroom Billiards, Phys. Rev. Lett. **103**, 154101 (2009).

[18] S. Shinohara, T. Harayama, T. Fukushima, M. Hentschel, S. Sunada, and E. E. Narimanov, Chaos-assisted emission from asymmetric resonant cavity microlasers, Phys. Rev. A **83**, 053837 (2011).

[19] J. Yang, S.-B. Lee, S. Moon, S.-Y. Lee, S. W. Kim, T. T. A. Dao, J.-H. Lee, and K. An, Pump-Induced Dynamical Tunneling in a Deformed Microcavity Laser, Phys. Rev. Lett. **104**, 243601 (2010).

[20] Y.-F. Xiao, X.-F. Jiang, Q.-F. Yang, L. Wang, K. Shi, Y. Li, Q. Gong, Tunneling-induced transparency in a chaotic microcavity, Laser Photonics Rev. **7**, L51 (2013).

[21] V. A. Podolskiy, E. Narimanov, W. Fang, and H. Cao, Chaotic microlasers based on dynamical localization, Proc. Natl. Acad. Sci. USA **101**, 10498 (2004).

[22] W. Fang, H. Cao, V. A. Podolskiy, and E. E. Narimanov, Dynamical localization in microdisk lasers, Opt. Express **13**, 5641 (2005).

[23] S. B. Lee, J. H. Lee, J. S. Chang, H. J. Moon, S. W. Kim, and K. An, Observation of Scarred Modes in Asymmetrically Deformed Microcylinder Lasers, Phys. Rev. Lett. **88**, 033903 (2002).

[24] N. B. Rex, H. E. Tureci, H. G. L. Schwefel, R. K. Chang, and A. D. Stone, Fresnel Filtering in Lasing Emission from Scarred Modes of Wave-Chaotic Optical Resonators, Phys. Rev. Lett. **88**, 094102 (2002).

[25] C. Gmachl, E. E. Narimanov, F. Capasso, J. N. Baillargeon, and A. Y. Cho, Kolmogorov-Arnold-Moser transition and laser action on scar modes in semiconductor diode lasers with deformed resonators, Opt. Lett. **27**, 824 (2002).

[26] J.-B. Shim, S.-B. Lee, S. W. Kim, S.-Y. Lee, J. Yang, and S. Moon, Uncertainty-Limited Turnstile Transport in Deformed Microcavities, Phys. Rev. Lett. **100**, 174102 (2008).

[27] S. B. Lee, J. Yang, S. Moon, S.-Y. Lee, S. W. Kim, J.-H. Lee, and K. An, Quasieigenstate evolution in open chaotic billiards, Phys. Rev. A **80**, 011802 (2009).

[28] M. V. Berry and M. Robnik, Semiclassical level spacings when regular and chaotic orbits coexist, J. Phys. A **17**, 2413 (1984).

[29] P. Gaspard and S. A. Rice, Semiclassical quantization of the scattering from a classically chaotic repellor, J. Chem. Phys. **90**, 2242 (1989).
[30] P. So, S. M. Anlage, E. Ott, and R. N. Oerter, Wave Chaos Experiments with and without Time Reversal Symmetry: GUE and GOE Statistics, Phys. Rev. Lett. **74**, 2662 (1995)
[31] E. N. Pozzo, D. Domínguez, and M. J. Sánchez, Quantum chaos in the mesoscopic device for the Josephson flux qubit, Phys. Rev. B **77**, 024518 (2008).
[32] J. Wiersig and J. Main, Fractal Weyl law for chaotic microcavities: Fresnel's laws imply multifractal scattering, Phys. Rev. E **77**, 036205 (2008).
[33] A. Potzuweit, T. Weich, S. Barkhofen, U. Kuhl, H.-J. Stöckmann, and M. Zworski, Weyl asymptotics: From closed to open systems, Phys. Rev. E **86**, 066205 (2012).
[34] S. Nonnenmacher and E. Schenck, Resonance distribution in open quantum chaotic systems, Phys. Rev. E **78**, 045202 (2008).
[35] M. Schönwetter and E. G. Altmann, Quantum signatures of classical multifractal measures, Phys. Rev. E **91**, 012919 (2015).
[36] E. Schenck, Weyl laws for partially open quantum maps, Ann. Henri Poincaré **10**, 711 (2009).
[37] E. G. Altmann, J. S. E. Portela, and T. Tél, Chaotic Systems with Absorption, Phys. Rev. Lett. **111**, 144101 (2013).
[38] L. Wang, D. Lippolis, Z.-Y. Li, X.-F. Jiang, Q. Gong, and Y.-F. Xiao, Statistics of chaotic resonances in an optical microcavity, Phys. Rev. E **93**, 040201(R) (2016); L. Wang, D. Lippolis, Z.-Y. Li, X.- F. Jiang, Q. Gong, and Y.-F. Xiao, Statistics of chaotic resonances in an optical microcavity, *ibid.* **94**, 029902 (2016).
[39] V. F. Lazutkin, *KAM Theory and Semiclassical Approximations to Eigenfunctions* (Springer-Verlag, Berlin, 1993).
[40] M. J. Davis and E. J. Heller, Quantum dynamical tunneling in bound states, J. Chem. Phys **75**, 246 (1981).
[41] G. Hackenbroich and J. U. Nöckel, Dynamical tunneling in optical cavities, Europhys. Lett. **39**, 371 (1997).
[42] K. Zyczkowski and H. J. Sommers, Truncations of random unitary matrices, J. Phys. A **33**, 2045 (2000).
[43] H. Schomerus and J. Tworzydlo, Quantum-to-Classical Crossover of Quasibound States in Open Quantum Systems, Phys. Rev. Lett **93**, 154102 (2004).
[44] W. T. Lu, S. Sridhar, and M. Zworski, Fractal Weyl Laws for Chaotic Open Systems, Phys. Rev. Lett. **91**, 154101 (2003).
[45] S. Nonnenmacher and M. Zworski, Fractal Weyl laws in discrete models of chaotic scattering, J. Phys. A **38**, 10683 (2005).
[46] H. Schomerus and Ph. Jacquod, Quantum-to-classical correspondence in open chaotic systems, J. Phys. A **38**, 10663 (2005).
[47] K. An and J. Yang, Mode-mode coupling theory of resonant pumping via dynamical tunneling processes in a deformed microcavity, in *Trends in Nano- and Micro-Cavities* (Bentham Science, Sharjia, UAE, 2011), pp. 40–61.
[48] K. An, Semiclassical theory of the many-atom microlaser, J. Korean Phys. Soc. **42**, 505 (2003).
[49] R. W. Boyd, *Nonlinear Optics* (Academic Press, Boston, 2009).
[50] U. Fano, Effects of configuration interaction on intensities and phase shifts, Phys. Rev. **124**, 1866 (1961).
[51] Q.-F. Yang, X.-F. Jiang, Y.-L. Cui, L. Shao, and Y.-F. Xiao, Dynamical tunneling-assisted coupling of high-Q deformed microcavities using a free-space beam, Phys. Rev. A **88**, 023810 (2013).
[52] Precisely, we suppose they are biorthogonal, given the non-Hermiticity of the Hamiltonian. See, for example, S.-Y. Lee, Decaying and growing eigenmodes in open quantum systems: Biorthogonality and the Petermann factor, Phys. Rev. A **80**, 042104 (2009).
[53] H. J. Stöckmann, *Quantum Chaos: An Introduction* (Cambridge University Press, Cambridge, 1999).
[54] M. J. Körber, M. Michler, A. Bäcker, and R. Ketzmerick, Hierarchical Fractal Weyl Laws for Chaotic Resonance States in Open Mixed Systems, Phys. Rev. Lett. **111**, 114102 (2013).
[55] A. Ishii, A. Akaishi, A. Shudo, and H. Schomerus, Weyl law for open systems with sharply divided mixed phase space, Phys. Rev. E **85**, 046203 (2012).
[56] J. Meiss, Symplectic maps, variational principles, and transport, Rev. Mod. Phys. **64**, 795 (1992).
[57] M. Michler, A. Bäcker, R. Ketzmerick, H.-J. Stöckmann, and S. Tomsovic, Universal Quantum Localizing Transition of a Partial Barrier in a Chaotic Sea, Phys. Rev. Lett. **109**, 234101 (2012).
[58] Y. C. Lai and T. Tél, *Transient Chaos* (Springer, New York, 2010).
[59] For a definition of free-spectral range in microresonators, see, for example, P. Rabiei and W. H. Steier, Polymer microring resonators, in *Optical Microcavities*, edited by K. Vahala (World Scientific, Singapore, 2004).
[60] J. R. Taylor, *An Introduction to Error Analysis* (University Science Books, Sauselito, CA, 1997).
[61] P. Jacquod and E. V. Sukhorukov, Breakdown of Universality in Quantum Chaotic Transport: The Two-Phase Dynamical Fluid Model, Phys. Rev. Lett. **92**, 116801 (2004).
[62] L. D. Landau and E. M. Lifshitz, *Quantum Mechanics–Non-Relativistic Theory* (Pergamon, Oxford, 1991).
[63] A. Bäcker, R. Ketzmerick, S. Löck, and L. Schilling, Regular-to-Chaotic Tunneling Rates Using a Fictitious Integrable System, Phys. Rev. Lett. **100**, 104101 (2008).
[64] M. Cai, O. Painter, and K. J. Vahala, Observation of Critical Coupling in a Fiber Taper to a Silica-Microsphere Whispering-Gallery Mode System, Phys. Rev. Lett. **85**, 74 (2000).